Nanoscale

PAPER

View Article Online
View Journal | View Issue

Cite this: *Nanoscale*, 2018, **10**, 11901

Intrinsic quantum anomalous hall effect in a two-dimensional anilato-based lattice†

Xiaojuan Ni, [a] Wei Jiang, [a] Huaqing Huang,[a] Kyung-Hwan Jin [a] and Feng Liu*[a,b]

Received 2nd April 2018,
Accepted 16th May 2018

DOI: 10.1039/c8nr02651c

rsc.li/nanoscale

Using first-principles calculations, we predict an intrinsic quantum anomalous Hall (QAH) state in a monolayer anilato-based metal–organic framework $M_2(C_6O_4X_2)_3$ (M = Mn and Tc, X = F, Cl, Br and I). The spin–orbit coupling of M d orbitals opens a nontrivial band gap up to 18 meV at the Dirac point. The electron counting rule is used to explain the intrinsic nature of the QAH state. The calculated nonzero Chern number, gapless edge states and quantized Hall conductance all confirm the nontrivial topological properties in the anilato-based lattice. Our findings provide an organic materials platform for the realization of the QAH effect without the need for magnetic and charge doping, which are highly desirable for the development of low-energy-consumption spintronic devices.

Introduction

The quantum anomalous Hall (QAH) effect usually requires a combination of magnetic polarization and spin–orbit coupling (SOC) to generate an integer Hall conductance without an external magnetic field.[1] Thin films of Cr and V doped $(Bi, Sb)_2Te_3$ have been experimentally prepared in which Cr and V serve as magnetic dopants.[2–4] A plateau in the Hall conductance in a range of gating voltage was observed in those thin films, signifying the QAH state. However, the experiments were conducted at extremely low temperature (30–50 mK) partly because of a very low magnetic ordering temperature even though the bulk energy gap of Bi_2Te_3 is considerably large.[5] Therefore, a great number of theoretical efforts have been devoted to proposing a new high-temperature QAH state in both inorganic and organic materials, with special attention paid to ferromagnetic topological systems[6–11] without the need for magnetic doping. Some of the predicted structures such as Ru halides have been experimentally synthesized.[11] However, most of the predicted systems are not intrinsic and require charge doping (either electron or hole doping) to move the Fermi level and/or have not been experimentally made.[6,7,9] Here, we theoretically predict an intrinsic QAH state in an already experimentally made metal–organic framework (MOF) consisting of an anilato-based lattice.

MOF is rapidly emerging as a unique class of organic/inorganic hybrid materials which can be straightforwardly self-assembled from their corresponding metal atoms with ligands.[12–14] For example, the ligand 2,5-dihydroxy-1,4-benzoquinone ($C_6O_4H_4$) and its homologues with substituents in positions 3 and 6 with F, Cl, Br and I can provide a binding site to metal atoms to form various MOFs. In a pioneering work, a layered honeycomb network $M_2(C_6O_4H_2)_3$, M = Mn and Cd, was experimentally synthesized by Weiss *et al.* in 1986.[15] Metal atoms are octahedrally surrounded by oxygen atoms of the deprotonated ligands with a metal-to-ligand ratio of 2 : 3. In the past three decades, many efforts have been made to promote additional properties in these anilato-based MOFs by taking advantage of the functionality of the metal atoms.[16–18] The anilato-based family $M_2(C_6X_2O_4)_3$ with a honeycomb structure has been extended to M = Cr, Mn, Fe, Co, Ni, Cu, Zn, Al, Ga and Ln with X = F, Cl, Br and I to tune the functionality, such as magnetic ordering temperature and electrical conductivity.[19–26] So far, only a few MOFs have been theoretically predicted to exhibit nontrivial topological properties[27–33] since the first organic Chern insulator reported in 2013.[34,35] Similar to the case of predicted inorganic topological materials, some of the predicted organic structures have not yet been synthesized in experiments[35] and some of them are not intrinsic.[30–32] Therefore, the focus of the present work is to propose experimental realization of the QAH effect in the already existing anilato-based $M_2(C_6X_2O_4)_3$ with neither magnetic nor charge doping.

Using density functional theory (DFT), we investigated the structural, electronic and topological properties of the anilato-based framework $Mn_2(C_6O_4Cl_2)_3$ lattice, as experimentally synthesized. A band gap of 13.8 meV at the Dirac point is opened

[a]*Department of Materials Science and Engineering, University of Utah, Salt Lake City, UT 84112, USA. E-mail: fliu@eng.utah.edu*
[b]*Collaborative Innovation Center of Quantum Matter, Beijing, 100084, China*
†Electronic supplementary information (ESI) available. See DOI: 10.1039/c8nr02651c

by SOC. The calculated nonzero Chern number, quantized Hall conductance, and edge states within the SOC gap all confirm the nontrivial topology. Remarkably, the QAH phase is intrinsic with the Fermi level exactly located within the topologically nontrivial SOC gap, which is analyzed and explained by the electron counting rule. We expand the anilato-based lattice into $M_2(C_6O_4X_2)_3$ (M = Mn and Tc, X = F, Cl, Br and I) to further achieve an SOC gap up to 18 meV.

Methods

The first principles calculations for structural stability, electronic and topological properties of $M_2(C_6O_4X_2)_3$ were carried out in the framework of the Perdew–Burke–Ernzerhof type generalized gradient approximation functional using the Vienna *ab initio* simulation package (VASP).[36] All the self-consistent calculations were performed with a plane-wave cutoff of 400 eV on a 5 × 5 × 1 Monkhorst–Pack *k*-point mesh in the supercells with the vacuum layer more than 15 Å thick to ensure the decoupling between the neighboring slabs. For the structural relaxation, all the atoms are allowed to relax until the atomic forces are smaller than 0.01 eV $Å^{-1}$.

Results and discussion

The anilato-based $M_2(C_6O_4X_2)_3$ lattice consists of metal atoms (Mn or Tc) and organic ligands (L), forming the L–M–L organometallic linkages with an octahedral coordination, as shown in Fig. 1. After structural relaxation of $Mn_2(C_6O_4Cl_2)_3$ in a free-standing state, the optimized lattice constant is 13.49 Å, which is comparable with the experimental value of 14.07 Å with a layered honeycomb structure.[20] The ferromagnetic state with a magnetic moment of $4.0\mu_B$ per unit cell is found energetically more favorable than the antiferromagnetic and nonmagnetic states. The antiferromagnetic state is found less stable than the ferromagnetic state by about 0.25 eV per unit cell. Using this energy difference as input, we estimated the Curie temperature by carrying out Monte Carlo simulations with the Ising model to investigate the magnetization energy as a function of temperature. The magnetic coupling Hamiltonian can be written as,

$$H = -J\sum_{\langle i,j\rangle}\frac{S_i}{|S|}\frac{S_j}{|S|}$$

where J is the exchange parameter, ($J = E_{ex}/3$ = 83 meV), S_i is the magnetic moment at site i, and S is the normalization factor of the magnetic moment. In the Monte Carlo simulations, we used a 50 × 50 super cell with the periodic boundary condition. At each temperature, 2×10^6 loops are taken to reach thermal equilibrium. The variations of the magnetic moment and energy per unit cell with respect to temperature are plotted in Fig. 2(a). The snapshots of spin configuration at 400 K and 1100 K are shown in Fig. 2(b) and (c), respectively. The system undergoes a transition from ferromagnetic to a paramagnetic state at about 735 K. Therefore, the experimental observation of QAH state will not be limited by a low magnetic transition temperature.

To further examine the stability of the $Mn_2(C_6O_4Cl_2)_3$ lattice, a 3 × 3 super cell containing 342 atoms was adopted to perform *ab initio* molecular dynamics simulations with the Nose–Hoover thermostat beginning at 300 K. As illustrated in Fig. 3, no destruction was found in the framework up to 3000 fs of simulation, which confirms the dynamical stability of the monolayer structure at room temperature.

The spin-polarized band structure along the high-symmetry k-path without SOC in Fig. 4a shows that the bands near the Fermi level are composed of two Dirac bands above a flat band, possessing the characteristic of a kagome band. The projected density of states (PDOS) shows that the states near the

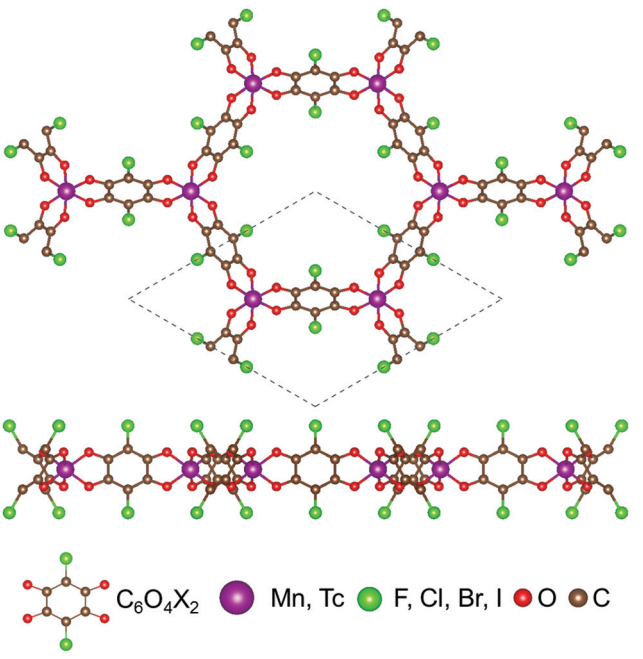

Fig. 1 Top and side views of the anilato-based $M_2(C_6O_4X_2)_3$ (M = Mn and Tc, X = F, Cl, Br and I) lattice. The rhombus with dashed lines shows the unit cell.

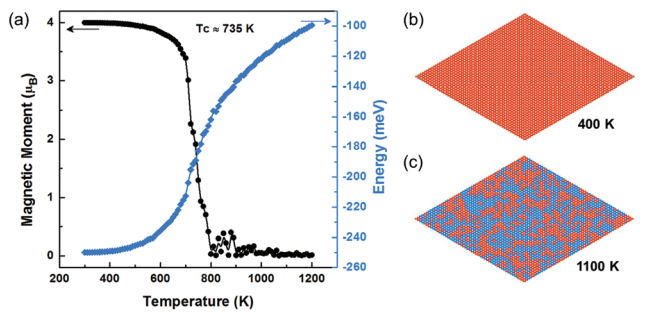

Fig. 2 (a) Monte Carlo simulations of the magnetic moment and energy per unit cell. The Curie temperature is found to be about 735 K. (b) and (c) are the spin configurations at 400 K and 1100 K, respectively. The red and blue colors indicate the spin-up and -down states, respectively.

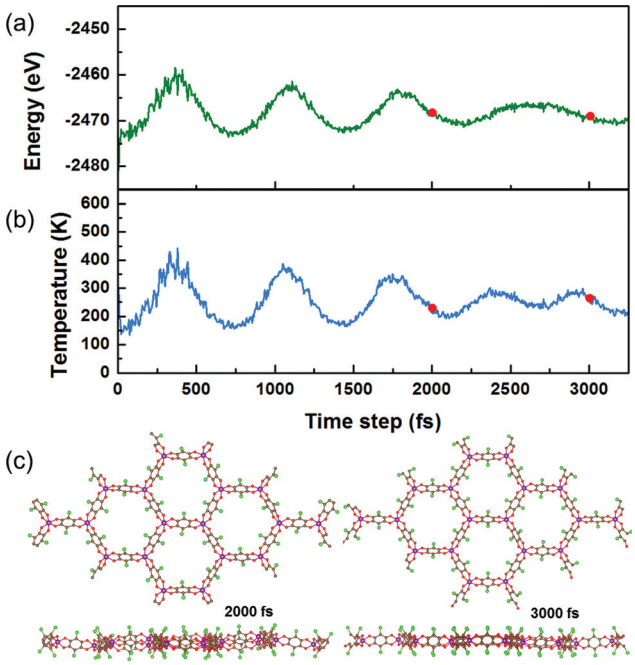

Fig. 3 Molecular dynamics simulation results. (a) Temperature and (b) energy fluctuations as a function of time. (c) Snap shots taken at 2000 fs and 3000 fs.

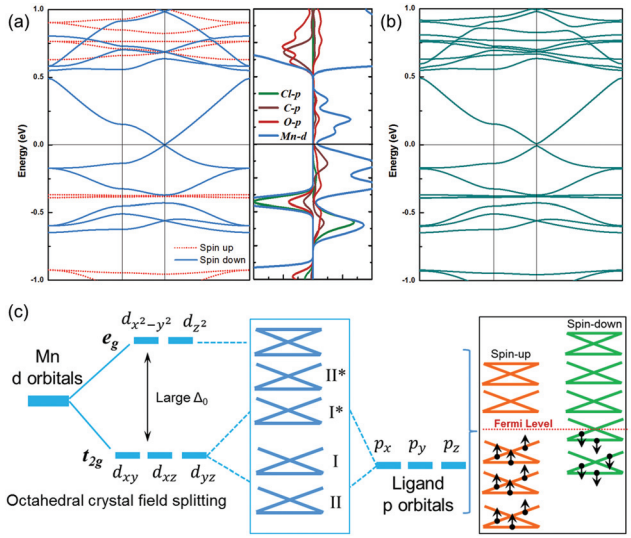

Fig. 4 $Mn_2(C_6O_4Cl_2)_3$ lattice: (a) band structure and PDOS without SOC. (b) Band structure with SOC. (c) Schematic illustrations of electron counting and orbital hybridization between Mn atoms and organic ligands.

Fermi level mainly come from the d orbitals of Mn, with little contribution from the p orbitals of ligands. After taking SOC into account, an energy band gap of 13.8 meV is opened at the Dirac point (Fig. 4b). A simple electron counting rule and orbital hybridization analysis were carried out to explain the intrinsic nature of the QAH state. The ligand is considered as a super-atom with two free radicals and it tends to accept electrons from its nearest neighboring metal atoms. A schematic illustration of the orbital hybridization between Mn and ligand is shown in Fig. 4c. The crystal field splits the five-fold degenerate d orbitals into threefold degenerate t_{2g} states and twofold degenerate e_g states in a nearly octahedral environment (see Table S1 in ESI†). The hybridization between Mn d orbitals and p orbitals of ligands leads to four groups of triple states: the bonding states (I and II) and the anti-bonding states (I* and II*). There are 14 valence electrons, 8 from Mn and 6 from ligands. Consequently, the state II* is empty while the state II is fully occupied with 6 electrons; 6 spin-up electrons occupy states I and I* and the other two spin-down electrons occupy state I with the Fermi level locating exactly at the Dirac point of state I. This gives a net magnetic moment $4\mu_B$, which is in accordance with the DFT results (Fig. S1†).

The spin-polarized electron density calculated from the charge difference between spin-up and spin-down channels in the ferromagnetic state is plotted in Fig. S2,† indicating that the major part of spin density comes from Mn. The interaction between magnetic moments connected through an intervening non-magnetic ligand with a relatively long distance can be explained in terms of superexchange[37] mediated by the ligands. The magnetic moments are strongly localized on the magnetic centers (Mn) and interact directly with the ligands. This induces a spin density on the ligands that is in the opposite direction to that of the spins on Mn, which can be directly seen from the calculated magnetization density distribution, as shown in Fig. S2.†

We note that the metal atoms locate at the hexagonal sites, while the bands near the Fermi level have the characteristics of the kagome band. The kagome band in a hexagonal lattice has been reported in a model graphene lattice made of sd2 hybridized transition metal atoms (W@Cl-Si(111)), which can be effectively renormalized into a single-orbital hopping on a kagome lattice.[38] In the present $Mn_2(C_6O_4Cl_2)_3$ lattice, the appropriate charge transfer from Mn to ligand facilitates an electron localization around the ligand as the charge center to form the kagome lattice, which can be distinctly seen from the electron localization function (ELF) in Fig. 5. The contour plots of ELF in Fig. 5c–e explicitly indicate that the center Mn hybridizes with the ligands through the octahedrally coordinated O atoms to distribute the electrons on a kagome lattice, which can effectively explain the kagome band near the Fermi level with the major contribution from Mn d orbitals.

We further employed the maximally localized Wannier functions (MLWFs) to fit the DFT band structure and calculate the edge states, Berry curvature and Hall conductance.[39,40] The bands fitted from the MLWFs in the energy window (E_{fermi} −0.1, E_{fermi} +0.1) eV shown in the right panel of Fig. 6a reproduce the DFT bands sufficiently well. Based on a recursive strategy, we constructed the edge Green's function of the semi-infinite lattice from the MLWFs and calculated the local density of the edge, as shown in Fig. 6b for one of the edges; the other edge is symmetric to this one. The bulk states are connected by the topologically nontrivial edge state and the number of edge states indicates the absolute value of the

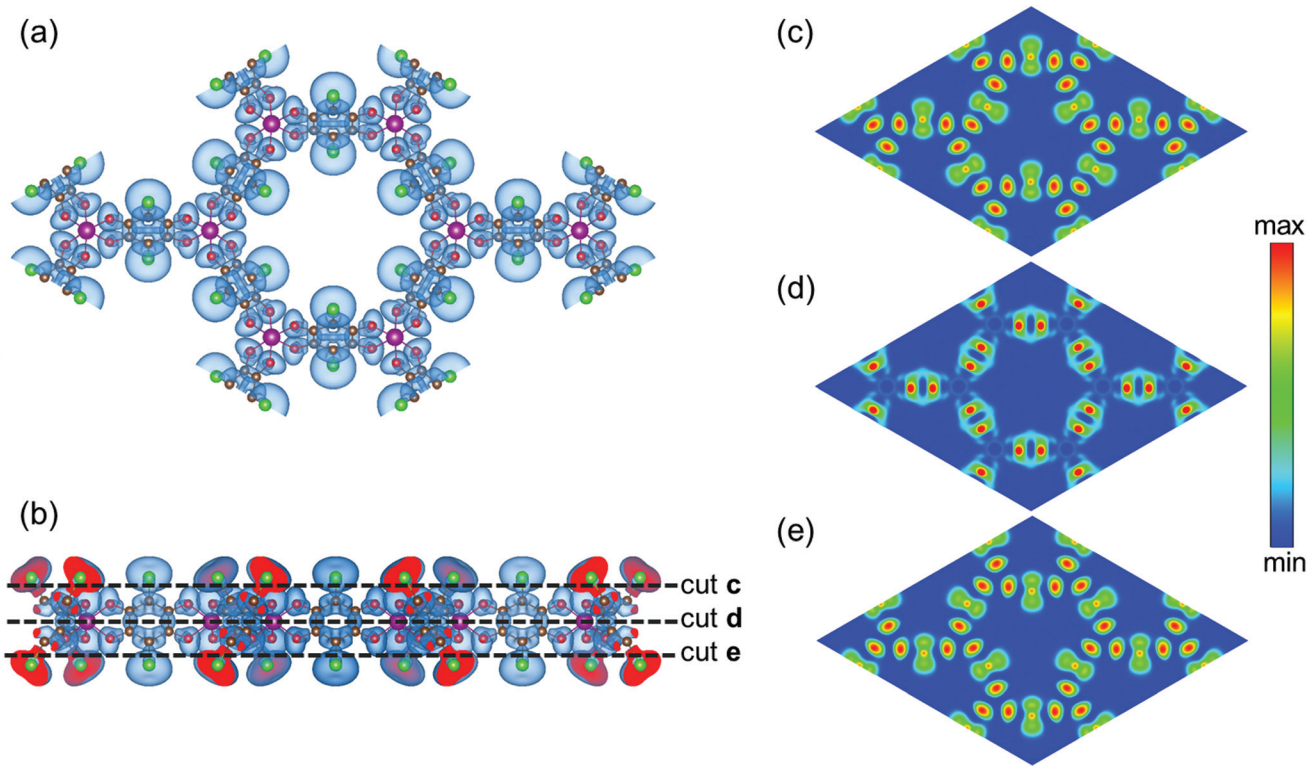

Fig. 5 Top (a) and side (b) views of electron localization function in the $Mn_2(C_6O_4Cl_2)_3$ lattice. (c) (d) and (e) are contour plots of the ELF along the cuts indicated in (b).

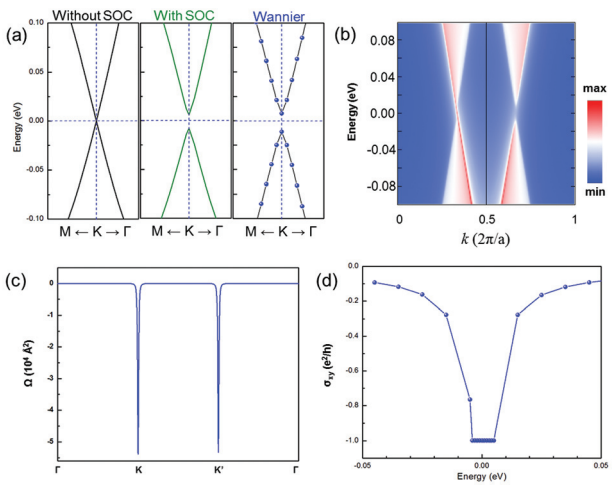

Fig. 6 The zoom-in band structure near the Fermi level without SOC, with SOC and fitted by MLWFs, respectively. (b) The semi-infinite Dirac edge states within the SOC gap. (c) Berry curvature for the occupied bands along the high symmetry directions. (d) Quantum anomalous Hall conductance as a function of the Fermi level, showing the quantized value within the SOC gap.

Chern number, which is $|C| = 1$. The Berry curvature for all the occupied bands along high-symmetry directions with nonzero values localized around K and K' points with the same sign shown in Fig. 6c. Integrating the Berry curvatures over the first Brillouin zone (BZ), the Chern number $C = -1$, with each Dirac cone contributing -0.5. Fig. 6d represents the calculated Hall conductance as a function of the Fermi level, which has a quantized value within the SOC gap, characterizing the signature of the QAH state.

To further illustrate the intrinsic nontrivial topology induced by SOC, we constructed a single-orbital tight-binding (TB) model to describe the kagome band near the Fermi level. For approximation, the TB Hamiltonian with intrinsic SOC and exchange field can be written as,

$$H = \varepsilon_0 - \left(t_1 \sum_{\langle i,j\rangle,\alpha} c_{i\alpha}{}^{+} c_{j\alpha} + t_2 \sum_{\langle\langle i,j\rangle\rangle,\alpha} c_{i\alpha}{}^{+} c_{j\alpha} + t_3 \sum_{\langle\langle\langle i,j\rangle\rangle\rangle,\alpha} c_{i\alpha}{}^{+} c_{j\alpha} + \text{h.c.} \right) + \frac{2i\lambda}{\sqrt{3}} \sum_{\langle ij\rangle} c_i{}^{+} \vec{s} \cdot \left(\frac{\vec{d}_{jk}}{|\vec{d}_{jk}|} \times \frac{\vec{d}_{ki}}{|\vec{d}_{ki}|} \right) c_j + M \sum_{i,\alpha,\beta} c_{i\alpha}{}^{+} s^{z}_{\alpha\beta} c_{i\beta}$$

where ε_0 is the on site energy for both spin-up and spin-down channels, $c_{i\alpha}{}^{+}$ and $c_{i\alpha}$ are the creation and annihilation operators for an electron with spin α on site i, respectively. Nearest-neighbor (NN), second-nearest-neighbor (2NN) and third-nearest-neighbor (3NN) hopping are denoted by $\langle ij\rangle$, $\langle\langle ij\rangle\rangle$ and $\langle\langle\langle ij\rangle\rangle\rangle$ with hopping parameters t_1, t_2 and t_3. The third term is the NN intrinsic SOC with magnitude λ, $\vec{s}$ is the spin Pauli matrix and $\vec{d}_{ki}$ is the vector from site i to site k. The last term is the exchange field with magnitude M. We note that only the spin-down bands near the Fermi level show the obvious topo-

logical nontrivial properties; hence we only focus on the spin-down states by taking the exchange field strength M sufficiently large to separate the spin-up and spin-down states.[35]

The band structure obtained through the above Hamiltonian reproduces the kagome band from the DFT calculation pretty well, as shown in Fig. 7a. To more clearly see the electronic band structure in a larger BZ containing more high symmetric points, we plot a three-dimensional band, as shown in Fig. 7b. There are six gapped Dirac cones at the zone corners. The Berry curvature distribution of the conduction and valence bands calculated from the TB model in Fig. 7c and d give the Chern number $C = 1$ and -1 by integrating the Berry curvature over the first BZ (marked out with the dashed hexagon), respectively. Therefore, both DFT calculations and the TB model have confirmed that the intrinsic SOC in the $Mn_2(C_6O_4Cl_2)_3$ lattice can induce the nontrivial topological properties to realize the QAH phase.

We also calculated the electronic and topological properties of other members from the anilato-based family $M_2(C_6O_4X_2)_3$ with X = F, Br and I (M = Mn), and M = Tc (X = Cl). Tc is a transition metal and can serve as metal centers by strong bridges with many organic ligands to form various complexes,[41] such as the experimentally synthesized $[Tc(CO)_3(MeCN)_3]ClO_4$,[42] $[TcBr_2(PMe_3)_4]$, $[Tc_2Br_4(PMe_3)_4]$ (ref. 43) and tricarbonyl complexes.[44] So we propose an anilato-based Tc lattice to achieve a larger topological nontrivial band gap. The correlation effect was examined for Mn, Tc (X = Cl). A ferromagnetic ground state for Mn (X = Cl) having a magnetic moment of $4.0\mu_B$ was obtained using the effective U_{eff} = 1.0 and 2.0 eV (parameters for onsite Coulomb interactions), same as the result using U = 0. As for Tc (X = Cl), the spin-up and spin-down bands cross at the Fermi level giving rise to a non-integer magnetic moment without U. For U_{eff} = 2.0 eV, the ground state of Tc (X = Cl) is ferromagnetic having a magnetic moment of $4.0\mu_B$. The band structures with SOC near the Fermi level for the extended lattices are shown in Fig. S3,† and each of them has an energy gap opened at the Dirac point. The Berry curvature for all the occupied bands for Tc (X = Cl) with the calculated Chern number $C = -1$ is shown in Fig. S3(f).† We also calculated the Chern number of X = F, Br and I (M = Mn) with the nonzero value of -1, confirming the existence of the QAH phase in the anilato-based lattice. The lattice parameter and energy gap are summarized in Table S2.† The size of the SOC gap depends on the nature of metal atoms since the density of states near the Fermi level mainly come from the d orbitals of M. The lattice parameter does not vary much with the substitution of X atoms due to the hollow position of X with negligible contribution to the lattice size.

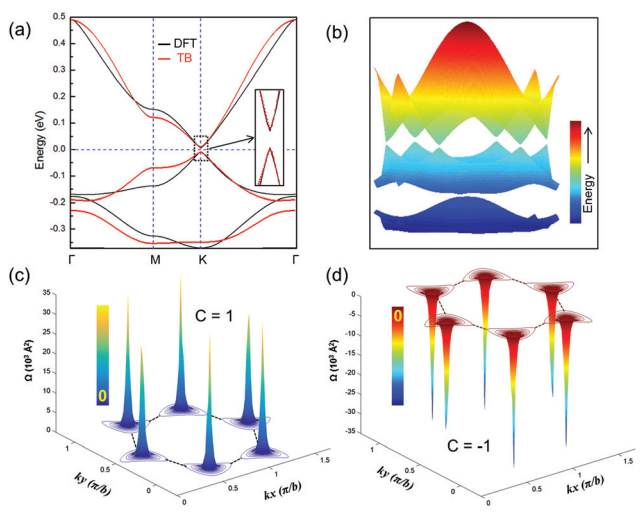

Fig. 7 (a) A comparison of band structure between DFT and the TB model. (b) 3D band structure from the TB model. (c) and (d) are the Berry curvatures in the first BZ for the conduction and valence bands with the Chern number C = 1 and -1.

Conclusions

In summary, the QAH state in a two-dimensional anilato-based $M_2(C_6O_4X_2)_3$ (M = Mn and Tc, X = F, Cl, Br and I) lattice is predicted by the DFT calculations and the TB model. This is the first report of the anilato-based lattice being able to realize the intrinsic QHA effect without additional magnetic and charge doping. Our findings are expected to expedite the experimental observation of the QAH phase in organic materials at relatively high temperatures.

Conflicts of interest

There are no conflicts to declare.

Acknowledgements

This work is supported by the DOE-BES (Grant No. DE-FG02-04ER46148). We acknowledge DOE-NERSC and CHPC at the University of Utah for providing the computing resources.

References

1 Z. F. Wang, K. Jin and F. Liu, *Wiley Interdiscip. Rev.: Comput. Mol. Sci.*, 2017, **7**, 1–19.
2 C. Chang, J. Zhang, X. Feng, J. Shen, Z. Zhang, M. Guo, K. Li, Y. Ou, P. Wei, L. Wang, Z. Ji, Y. Feng, S. Ji, X. Chen, J. Jia, X. Dai, Z. Fang, S. Zhang, K. He, Y. Wang, L. Lu, X.-C. Ma and Q.-K. Xue, *Science*, 2013, **340**, 167–171.
3 X. Kou, S. Guo, Y. Fan, L. Pan, M. Lang, Y. Jiang, Q. Shao, T. Nie, K. Murata, J. Tang, Y. Wang, L. He, T. Lee, W. Lee and K. L. Wang, *Phys. Rev. Lett.*, 2014, **137201**, 1–5.
4 C. Chang, W. Zhao, D. Y. Kim, H. Zhang, B. A. Assaf, D. Heiman, S. Zhang, C. Liu, M. H. W. Chan and J. S. Moodera, *Nat. Mater.*, 2015, **14**, 473–477.
5 Y. L. Chen, J. G. Analytis, J.-H. Chu, Z. K. Liu, S.-K. Mo, X. L. Qi, H. J. Zhang, D. H. Lu, X. Dai, Z. Fang, S. C. Zhang,

I. R. Fisher, Z. Hussain and Z.-X. Shen, *Science*, 2009, **325**, 178–181.
6 Z. Qiao, W. Ren, H. Chen, L. Bellaiche, Z. Zhang, A. H. MacDonald and Q. Niu, *Phys. Rev. Lett.*, 2014, **112**, 1–5.
7 S. C. Wu, G. Shan and B. Yan, *Phys. Rev. Lett.*, 2014, **113**, 1–5.
8 Y. Wang, Z. Wang, Z. Fang and X. Dai, *Phys. Rev. B: Condens. Matter Mater. Phys.*, 2015, **91**, 3–10.
9 X. Zhang and M. Zhao, *RSC Adv.*, 2015, **5**, 9875–9880.
10 W. Ji, B. Zhang, S. Zhang, C. Zhang, M. Ding, P. Li and P. Wang, *J. Mater. Chem. C*, 2017, **5**, 8504–8508.
11 C. Huang, J. Zhou, H. Wu, K. Deng, P. Jena and E. Kan, *Phys. Rev. B*, 2017, **95**, 1–7.
12 S. Li and F. Huo, *Nanoscale*, 2015, **7**, 7482–7501.
13 T. Kambe, R. Sakamoto, T. Kusamoto, T. Pal, N. Fukui, K. Hoshiko, T. Shimojima, Z. Wang, T. Hirahara, K. Ishizaka, S. Hasegawa, F. Liu and H. Nishihara, *J. Am. Chem. Soc.*, 2014, **136**, 14357–14360.
14 X. Sun, K.-H. Wu, R. Sakamoto, T. Kusamoto, H. Maeda, X. Ni, W. Jiang, F. Liu, S. Sasaki, H. Masunagae and H. Nishihara, *Chem. Sci.*, 2017, **8**, 8078–8085.
15 A. Weiss, E. Riegler and C. Robl, *Z. Naturforsch., B: Anorg. Chem., Org. Chem.*, 1986, **41**, 1501–1505.
16 M. Atzori, S. Benmansour, M. Guillermo, M. Clemente-leo, A. Abherve, P. Go, E. Coronado, F. Artizzu, E. Sessini, P. Deplano, A. Serpe, M. L. Mercuri and C. J. Go, *Inorg. Chem.*, 2013, **52**, 10031–10040.
17 S. Benmansour, C. Valle and C. J. Go, *Inorg. Chem.*, 2015, **54**, 5410–5418.
18 T. Hydranilato, M. Iii, C. Metallotectons, M. Atzori, L. Marchio, R. Cle, A. Serpe, P. Deplano, N. Avarvari and M. L. Mercuri, *Cryst. Growth Des.*, 2014, **14**, 5938–5948.
19 S. Benmansour, P. Go, C. Valle, M. Guillermo and C. J. Go, *Cryst. Growth Des.*, 2016, **16**, 518–526.
20 S. Aldoshin, R. Academy, V. Makhaev, R. Academy and A. Mossbauer, *Russ. Chem. Bull.*, 2011, **60**, 1–11.
21 C. J. Kingsbury, B. F. Abrahams, D. M. D. Alessandro, T. A. Hudson, R. Murase, R. Robson and K. F. White, *Cryst. Growth Des.*, 2017, **17**, 1465–1470.
22 J. A. Degayner, I. Jeon, L. Sun, M. Dinca and T. D. Harris, *J. Am. Chem. Soc.*, 2017, **139**, 4175–4184.
23 T. Luo, Y. Liu, H. Tsai, C. Su, C. Ueng and K. Lu, *Eur. J. Inorg. Chem.*, 2004, **2**, 4253–4258.
24 S. Halis, A. K. Inge, N. Dehning, T. Weyrich, H. Reinsch and N. Stock, *Inorg. Chem.*, 2016, **55**, 7425–7431.
25 S. Benmansour, A. Hernández-paredes and C. J. Gómez-garcía, *J. Coord. Chem.*, 2017, 1–19.
26 M. L. Mercuri, F. Congiu and G. Concas, *Magnetochemistry*, 2017, **3**, 1–56.
27 Z. F. Wang, Z. Liu and F. Liu, *Nat. Commun.*, 2013, **4**, 1–5.
28 Z. F. Wang, N. Su and F. Liu, *Nano Lett.*, 2013, **13**, 2842–2845.
29 L. Z. Zhang, Z. F. Wang, B. Huang, B. Cui, Z. Wang, S. X. Du and F. Liu, *Nano Lett.*, 2016, **16**, 2072–2075.
30 Y. Chen and Q. Sun, *J. Chem. Phys.*, 2017, **147**, 1–6.
31 X. Zhang, Z. Wang, M. Zhao, F. Liu and P. Gr, *Phys. Rev. B*, 2016, **93**, 1–5.
32 M. Zhao, A. Wang and X. Zhang, *Nanoscale*, 2013, **5**, 10404–10408.
33 Y. P. Wang, W. X. Ji, C. W. Zhang, P. Li, P. J. Wang, B. Kong, S. S. Li, S. S. Yan and K. Liang, *Appl. Phys. Lett.*, 2017, **110**, 1–5.
34 Z. Liu, Z. F. Wang, J. W. Mei, Y. S. Wu and F. Liu, *Phys. Rev. Lett.*, 2013, **110**, 1–5.
35 Z. F. Wang, Z. Liu and F. Liu, *Phys. Rev. Lett.*, 2013, **110**, 1–5.
36 G. Kresse and J. Hafner, *Phys. Rev. B: Condens. Matter Mater. Phys.*, 1993, **47**, 558(R).
37 E. Coronado, P. Delhaès, D. Gatteschi and J. S. Miller, *Molecular Magnetism: From Molecular Assemblies to the Devices*, Springer, Dordrecht, 1996.
38 M. Zhou, Z. Liu, W. Ming, Z. Wang and F. Liu, *Phys. Rev. Lett.*, 2014, **113**, 1–5.
39 A. A. Mostofi, J. R. Yates, Y. Lee, I. Souza, D. Vanderbilt and N. Marzari, *Comput. Phys. Commun.*, 2008, **178**, 685–699.
40 Q. S. Wu, S. N. Zhang, H. F. Song, M. Troyer and A. A. Soluyanov, *Comput. Phys. Commun.*, 2017, **224**, 405–416.
41 D. Hernández-Valdés, R. Alberto and U. Jáuregui-Haza, *RSC Adv.*, 2016, **6**, 107127–107140.
42 A. E. Miroslavov, G. V. Sidorenko, A. A. Lumpov, D. N. Suglobov, O. V. Sizova, D. A. Maltsev, V. V. Gurzhiy and Y. S. Polotskii, *J. Organomet. Chem.*, 2012, **720**, 1–6.
43 F. Poineau, P. F. Weck, P. M. Forster, A. P. Sattelberger and K. R. Czerwinski, *Dalton Trans.*, 2009, 10338–10342.
44 C. Moura, C. Fernandes, L. Gano, A. Paulo, I. C. Santos, I. Santos and M. J. Calhorda, *J. Organomet. Chem.*, 2009, **694**, 950–958.

